Chapter 5

Metal Oxides-Manganese Oxide Nanocomposites and their Applications in Electrocatalysis and Cytotoxicity Studies

5.1. Fe_3O_4- Mn_3O_4 Nanocomposites for Cytotoxicity Studies

5.1.1. Introduction

The integration of nanotechnology with molecular biology has emerged as nanobiotechnolgy that has pioneered exciting opportunities for discovering new materials, processes, and phenomena.[1] At the present age of human civilisation, due to increased stress conditions, mind and body are, significantly, making an impact on the immune system that is responsible for the etiologic as well as pathologic mechanisms of various diseases.[2] It is, now, well established from animal studies that macrophages play an important role in the defence mechanism against host infection by innate and acquired immunity.[3] Macrophages are robust cells, known for their capability to kill pathogens or kill altered self-cells, *viz.*, tumor cells or virus infected cells or trigger lymphocytes to produce antibodies during the development of specific immunity and also increase the phagocytic activity and inflammatory responses in eliminating foreign matter.[3] In the process of phagocytosis, the macrophages produce cytokines, reactive oxygen species (ROS) and nitrogen species (RNS) that are involved in the destruction of pathogens. To overcome the immunosupression and immunodepression that would hamper the resistivity against pathogens, cell viability and cytotoxicity assays are used for screening of certain chemicals that are able to destroy living cells. Based on these perspectives, the ability to accurately measure cytotoxicity is indispensable in identifying compounds that might pose certain health risks in humans and in the process of developing therapeutic anti-cancer drugs.[4]Magnetic nanoparticles have engendered potential applications in biology and medicine, including, magnetic bioseparation and biosensing, medical diagnosis and therapy, targeted drug delivery and biological labels.[5] Amongst the lexicon of magnetic nanoparticles, the superparamagnetism of magnetite along with low toxicity and excellent biocompatibility has fascinated these particles in a myriad of biological events.[6] However, it has been experienced that the iron oxide nanoparticles synthesised as colloidal dispersion are highly magnetic and hydrophobic in nature that render their inherent tendency to agglomerate and limit their utility in numerous biomedical applications.[7] To impart stability and ensure nontoxicity under physiological conditions, researchers have often adopted the concept of molecular functionalisation with judiciously selected proper ligands, which ideally should have a

high affinity for the iron oxide core, be nonimmunogenic and nonantigenic and prevent opsonisation by plasma proteins.[6,8] On the other hand, the conjugation of magnetic nanoparticles with quantum dots or metallic components produces nanocomposites with enhanced dispersity and provides a platform for improved medical imaging and controlled drug delivery, respectively.[9] As the third avenue to these two well-reputed roadmaps, the coupling of superparamagnetic Fe_3O_4 with relatively weak magnetic species could pave an effective strategy to avoid the tendency to agglomeration in colloidal dispersion.

In this sub-section, we have demonstrate that reduced magnetism through the formation of Fe_3O_4–Mn_3O_4 nanocomposites could offer a viable platform for *in-vitro* cytotoxicity determination on splenic macrophages in cell culture of mice.The advantages of maneuvering of Fe_3O_4–Mn_3O_4 nanocomposites are three folds: first, moderate magnetism to ensure good water dispersibility, colloidal stability and non-toxicity under physiological conditions; second, cytocompatibility of the average size distribution of the particles and third, benign and cost-effective synthetic strategy.

5.1.2. Experimental

5.1.2.1. Synthesis of Fe_3O_4 Nanoparticles

Polyethylene glycol-stabilized (PEG with hydroxyl end groups have been used, named PEG-13) iron oxide nanoparticles have been synthesised by mixing 1:2 molar ratio of Fe^{2+} : Fe^{3+} by following the method reported by Gillich et al.[10] In a typical synthesis, 1.99 g $(NH_4)_2Fe(SO_4)_2.6H_2O$ and 5.41 g $FeCl_3.6H_2O$ were dissolved in 50 ml distilled water in a beaker. In a separate beaker, an aqueous NH_4OH (30% w/w) solution was prepared. After that, polyethylene glycol (18.6 g) was added at a ratio of M : L = 1 : 10 (9.3 g each) to both the above solutions to get precursor solutions I and II respectively. Then, precursor solution II was added to solution I dropwise under stirring condition at 40 ^{0}C. Just after mixing the solutions, color of the solution changes from light brown to black indicating the formation of Fe_3O_4 nanoparticles. The stirring was continued for another 45 min. The precipitate so obtained was washed thrice by centrifugation and redispersion in distilled water. Finally, the as-obtained precipitate was dispersed in distilled water and stored in the vacuum desiccator.

5.1.2.2. Synthesis of Fe_3O_4—Mn_3O_4 Nanocomposites

Dual magnetic metal oxide nanocomposites have been synthesised by alkaline hydrolysis of manganese precursor in the presence of as-synthesised Fe_3O_4 nanoparticles as shown in Scheme 5.1. In a typical synthesis, 1.0 ml aqueous dispersion of as-synthesised Fe_3O_4 nanoparticles (0.01 mmol) was added to an aqueous solution containing 0.1 mmol of $Mn(ac)_2.4H_2O$ so as to maintain the final volume to 25 ml in a double-necked round bottom flask. The faint yellow colour reaction mixture was stirred for 30 min at room temperature and subsequently, hydrolysed at 65^{o}C. Initially, when the temperature was reached to 50 ^{o}C, ammonium hydroxide solution (30%, 2.0 ml) was added dropwise and a distinct colour change from faint yellow to brownish red was seen. The heating and stirring was continued for another 90 min. After that, the reaction mixture was cooled down to room temperature and stirring was continued overnight. The brownish red colour dispersion so obtained was washed thrice by centrifugation and redispersion in distilled water. Finally, the as-obtained precipitate was dispersed in distilled water and stored in the vacuum desiccator.

Scheme 5.1. Schematic presentation for the synthesis of Fe_3O_4-Mn_3O_4nanocomposites.

5.1.3. Results and Discussion

In this experiment, Fe_3O_4–Mn_3O_4 nanocomposites have been synthesised by alkaline hydrolysis of manganese precursor in the presence of preformed polyethylene glycol-stabilised Fe_3O_4nanoparticles. The nanostructures have been examined by absorption spectroscopy, Fourier transform infrared spectroscopy, transmission electron microscopy, high resolution transmission electron microscopy, dynamic light scattering, selected area electron diffraction pattern, scanning electron microscopy,

energy dispersive X-ray analysis, elemental mapping, X-ray diffraction pattern, Raman spectroscopy, thermogravimetric analysis and vibrating sample magnetometry.

5.1.3.1. Absorption Spectra Analysis and Band Gap

Further insights into the nanocomposites have been augmented from multiple control experiments. Absorption measurements and band gap determination of Fe_3O_4 NPs and Fe_3O_4─Mn_3O_4 NCs reveal the electronic interaction amongst the components in the nanocomposites.[14]The absorption spectral features of Fe_3O_4 NPs and Fe_3O_4-Mn_3O_4NCs in the solid state and determination of their band gap are described in Fig. 5.1. Panel A shows the solid state absorption spectra of Fe_3O_4 NPs and Fe_3O_4-Mn_3O_4NCs. The electronic absorption spectrum of Fe_3O_4 NPs shows three well-defined regions: the first portion below 400 nm, the second from 400 to 550 nm and

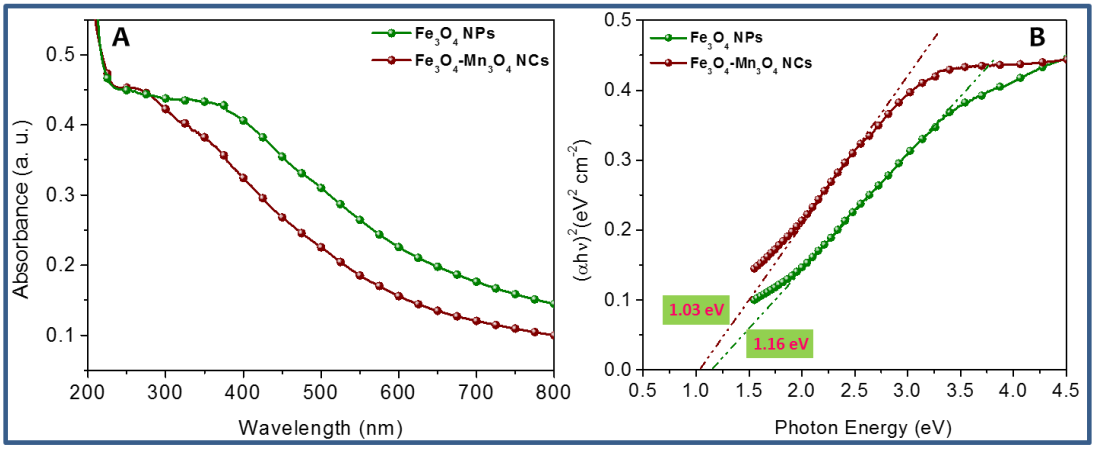

Fig. 5.1. (a) Absorption spectra in the solid state and (b) plot of $(\alpha h\nu)^2$ as a function of hν of Fe_3O_4 NPs and Fe_3O_4–Mn_3O_4 NCs.

the third one finishing at 800 nm. The first portion is assigned to the allowed $O^{2-} \rightarrow Fe^{2+}$ and $O^{2-} \rightarrow Fe^{3+}$ charge transfer transitions, and the last two can be reasonably related to d-d crystal-field transitions, $^3E_g(G) \leftarrow {}^3T_{1g}$, $^3A_{2g}(F) \leftarrow {}^3T_{1g}$, $^3A_{2g}(G) \leftarrow {}^3T_{1g}$, $^3T_{2g}(H) \leftarrow {}^3T_{1g}$, $^3T_{1g}$ (H) $\leftarrow {}^3T_{1g}$, and $^3E_g(H) \leftarrow {}^3T_{1g}$, on octahedral Fe^{3+} species.[11]Upon addition of manganese precursor and subsequent hydrolysis, the absorption spectrum corresponding to Fe_3O_4 NPs become perturbed indicating the electronic interaction amongst the individual components in the formation of nanocomposites.[12]The original color of Fe_3O_4 particles is brown as seen in the present experiment and that of Mn_3O_4 particles is yellowish brown, while the resulting Fe_3O_4-

Mn_3O_4 nanocomposites is reddish brown. This suggests that the finally formed Fe_3O_4-Mn_3O_4 nanocomposites have inherited the colorimetric character of Fe_3O_4 nanoparticles. The direct band gap energy (E_g) of the Fe_3O_4 NPs and Fe_3O_4─Mn_3O_4 NCs could be determined by fitting the absorption data to the direct band gap transition equation as,[13]

$$(\alpha h\nu)^2 = A(h\nu - E_g) \quad (5.1.)$$

where, α is the absorption co-efficient, $h\nu$ the photon energy and A a constant. The absorption coefficient (α) is defined as: $\alpha = 2.303\ A/L\ c$, where, A is the absorbance of the sample, c the loading of sample (g L^{-1}), L the path length (= 1 cm). From the profiles showing the plot of $(\alpha h\nu)^2$ as a function of $h\nu$(panel B), the estimated direct band gap of the Fe_3O_4 NPs and Fe_3O_4─Mn_3O_4 NCs was found to be 1.16 eV and 1.03 eV respectively; these values are considerably different from the reported value(~0.1 eV) of bulk Fe_3O_4.[14]

5.1.3.2. Fourier Transform Infrared Spectra of Fe_3O_4 NPs and Fe_3O_4–Mn_3O_4 NCs

A comparative Fourier transform infrared spectrum of Fe_3O_4 NPs andFe_3O_4–

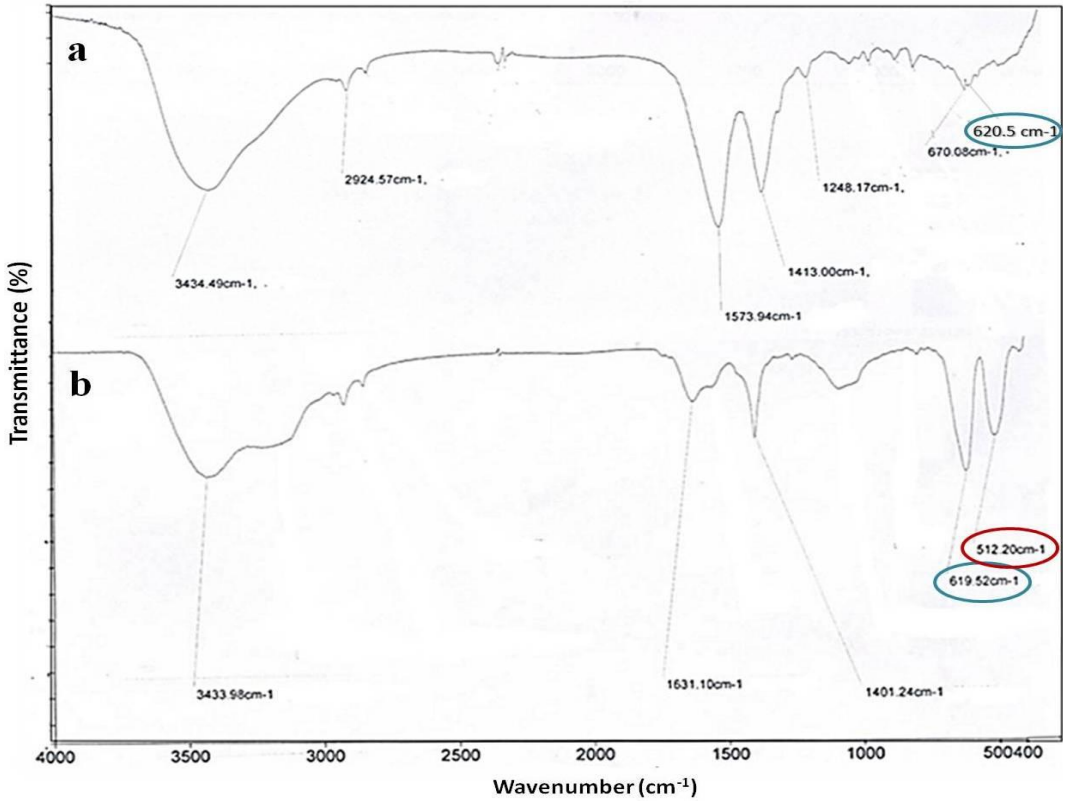

Fig. 5.2. Fourier transform infrared spectrum of the as-prepared (A) Fe_3O_4 NPs and (B) Fe_3O_4─Mn_3O_4 NCs.

Mn_3O_4 NCs is shown Fig. 5.2. The sample was heated at 800 ^{0}C in argon atmosphere for 1 h prior to measurement. Trace ais for Fe_3O_4 NPs; lower region band at 620 cm^{-1}can be attributed Fe─O vibrations. A broad band at around 3434 cm^{-1} can be for stretching vibration of –OH groups of polyethylene glycol which binds with Fe_3O_4 nanoparticles[15]Trace b represents that of as-prepared Fe_3O_4─Mn_3O_4 NCs. The presence of two bands at the low frequency region at 512 and 619 cm^{-1} can, clearly, be attributed to the Mn─O and Fe─O vibrations, respectively, confirming the presence of both the species in the composites The peak obtained at 1631 cm^{-1} is associated with C = O stretching and the peak at 1401 cm^{-1} is probably related to scissoring and bending of C─H.[16]The broad band at higher region around 3430 cm^{-1} is due to the stretching vibrations of polyethylene glycol present in the NCs with high intramolecular hydrogen bonding [17]

5.1.3.3. Raman Spectrum of Fe_3O_4-Mn_3O_4 NCs

The room temperature Raman spectrum of Fe_3O_4─Mn_3O_4 nanocomposites on silicon substrate with excitation at 488 nm (2.55 eV) of 5 mW air cooled Ar^+ laser is shown in Fig. 5.3. It is well established in the literature that the Raman spectrum of Mn_3O_4exhibits five phonon peaks: a (triply degenerate) T_{2g} symmetry mode at 290 cm^{-1}, a (doubly degenerate) E_g symmetry mode at 320 cm^{-1}, T_{2g} symmetry modes at 375 cm^{-1} and 479 cm^{-1}, and a (singly degenerate) A_{1g} symmetry "breathing" mode at 660 cm^{-1} while the Raman spectrum of Fe_3O_4 exhibits a prominent band centered near 670 cm^{-1} associated with the A_{1g} phonon mode of Fe_3O_4 with inverse spinel structure. In the present experiment, weaker signals located at 311, 368 and 511 cm^{-1} and strong signal at 655 cm^{-1} are seen. It is, therefore, apparent that the peak positions are, substantially, shifted to that of the original positions which indicates the formation of Fe_3O_4─Mn_3O_4 nanocomposites.[18,19]

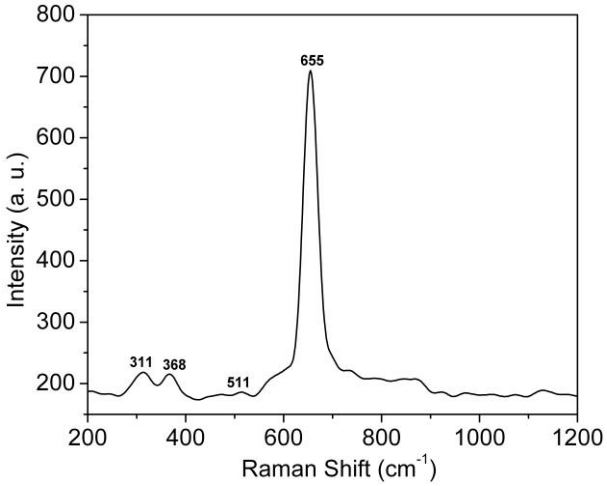

Fig. 5.3. Raman spectrum of Fe_3O_4-Mn_3O_4 nanocomposites

5.1.3.4. X-ray Diffraction Patterns of Fe_3O_4 NPs and Fe_3O_4-Mn_3O_4 NCs

For structural characterization of synthesized materials, a comparative X-ray diffraction pattern of Fe_3O_4 NPs and Fe_3O_4–Mn_3O_4 nanocomposites is shown in Fig. 5.4. Trace a is of the iron oxide nanoparticles. The presence of all the diffraction peaks implying a crystalline structure that can be indexed to the presence of inverse spinel structure of magnetite (JCPDS# 89-0691). The X-ray diffraction patterns of the as-prepared Fe_3O_4─Mn_3O_4 NCs in comparison with Fe_3O_4 have been illustrated in. The presence of all the diffraction peaks implying a crystalline structure that can be indexed to the presence of inverse spinel structure of magnetite (JCPDS# 89-0691) and tetragonal hausmannite (JCPDS# 24-0734) with space groups F_{d3m} and $I4_{I/amd}$, respectively, which indicates that preformed magnetite favours the formation of an ordered and single phase of Mn_3O_4 in the nanocomposites.[20-21]

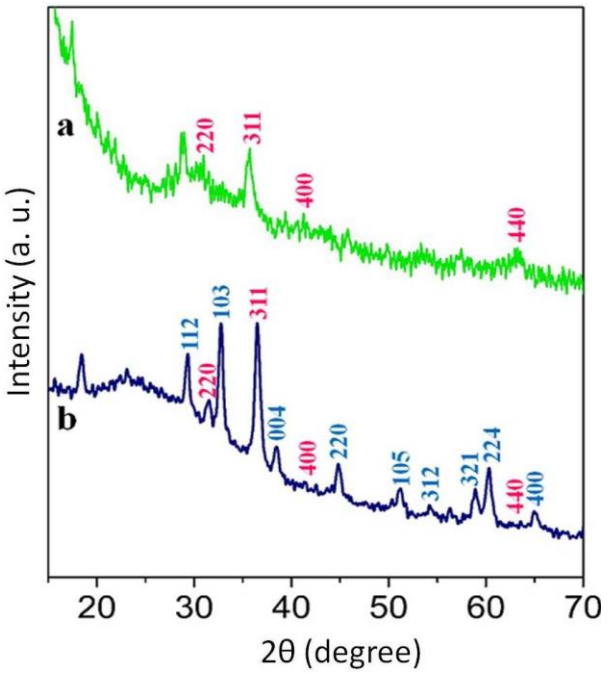

Fig. 5.4. X-ray diffraction patterns of (a) Fe_3O_4 NPs and (b) Fe_3O_4–Mn_3O_4 NCs

5.1.3.5. Morphology, Composition and Crystallinity of the Fe_3O_4 NPs and Fe_3O_4-Mn_3O_4 NCs

Fig. 5.5 represents the representative transmission electron micrographs of Fe_3O_4 (panel a) and Fe_3O_4─Mn_3O_4 (panel b) exhibit that the particles are spherical or nearly spherical with average diameter 8±1 and 12±2 nm, respectively. Inset in panel b shows that the number distribution hydrodynamic diameter of Fe_3O_4─Mn_3O_4 NCs is *ca.*15±5 nm. The small discrepancy in the particle size obtained from TEM and DLS measurements could be attributed to factors associated with the high vacuum conditions of TEM and the hydrodynamic and electrokinetic effects operative in DLS measurements.[22]Selected area electron diffraction pattern of the Fe_3O_4 nanoparticles (panel c) exhibits five diffraction rings of (220), (311), (420), (511) and (440) that

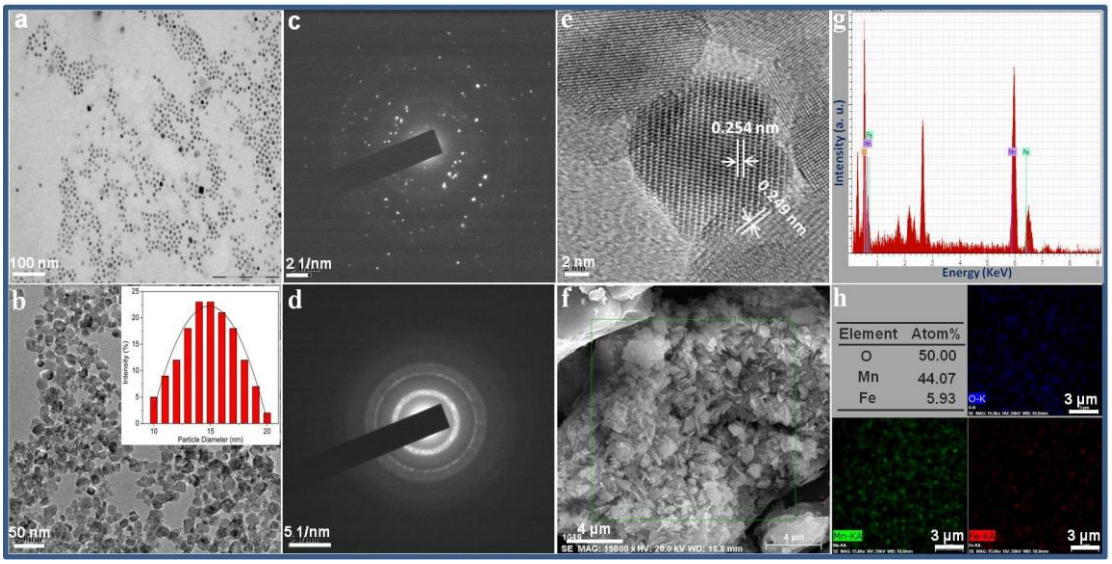

Fig. 5.5. (a, b) Representative transmission electron micrographs and (c, d) selected area electron diffraction patterns of Fe_3O_4 nanoparticles and Fe_3O_4–Mn_3O_4 nanocomposites, respectively; (e) high resolution transmission electron micrograph (f) scanning electron micrograph, (g) energy dispersive X-ray spectrum and (h) elemental mapping of Fe_3O_4–Mn_3O_4 nanocomposites. Inset in panel b shows the dynamic light scattering spectrum of the Fe_3O_4–Mn_3O_4 nanocomposites.

confirm a typical magnetite crystalline structure.[23]Selected area electron diffraction pattern of the Fe_3O_4─Mn_3O_4 nanocomposites (panel d) is consistent with diffraction rings of magnetite as well as tetragonal Mn_3O_4 with strong ring patterns due to (101), (103) and (220) planes. The observation of distinct ring patterns in the nanocomposites implies that the presence of preformed magnetite favours the formation of an ordered and single phase of Mn_3O_4 in the nanocomposites. High resolution transmission electron micrograph (panel e) of Fe_3O_4─Mn_3O_4 nanocomposites displays two distinct lattice spacings of 0.254 nm resulting from a group of (111) planes of Fe_3O_4[24]and 0.249 nm which corresponds to the distance between the (211) planes of the Mn_3O_4[25] tetragonal crystal lattice. Scanning electron micrograph of the nanocomposites (panel f) exhibits large grain structure having regular flake-like morphology which is, possibly, arising due to soft agglomerations upon drying of the magnetic particles onto the silicon wafer. Representative energy dispersive X-ray spectrum of Fe_3O_4─Mn_3O_4 nanocomposites (panel g) reveals that the particles are composed of Fe, Mn and O elements. Elemental mapping of the nanocomposites (panel h) exhibits the appearance of the blue, green and red coloured micrographs revealing the presence of oxygen (O), manganese (Mn) and iron (Fe) respectively.

5.1.3.6. Thermogravimetric Analysis of Fe_3O_4 -Mn_3O_4 Nanocomposites

Thermogravimetric analysis (Fig. 5.6.) of the as-dried powder sample shows two weight loss steps in the curve: 1.9 wt% loss corresponding to the water desorption (up to 200 °C), and a weight loss of 8.7 wt % over 200─800 ºC as a result of the decomposition of the polymer, verifying that the polyethylene glycol molecules employed for the stabilisation of Fe_3O_4 nanoparticles are, even, incorporated into the nanocomposites.[26]

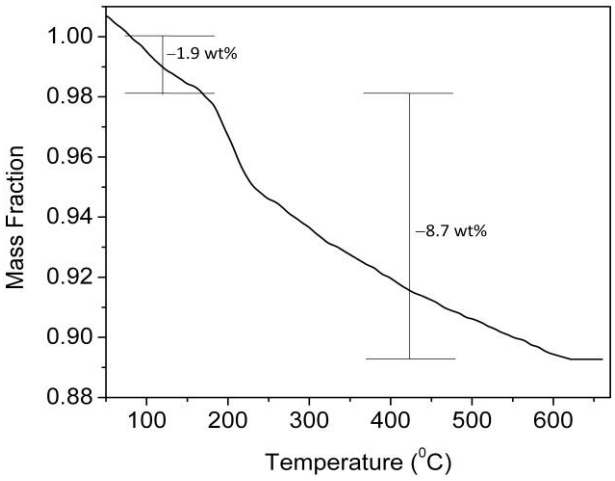

Fig. 5.6. Thermogravimetric analysis of Fe_3O_4–Mn_3O_4 nanocomposites as-dried in air

5.1.3.7.The Magnetic Hysteresis Curves of Fe_3O_4 NPs and Fe_3O_4─Mn_3O_4 NCs

The magnetic hysteresis curves of the as-prepared Fe_3O_4 NPs and Fe_3O_4─Mn_3O_4 NCs over the range of $-15 < H < 15$ kOe at room temperature are presented in Fig. 5.7. It is seen that the both types of particles are superparamagnetic; the saturation magnetisation of Fe_3O_4 NPs and Fe_3O_4─Mn_3O_4 NCs are 24.97 and 14.26 emu g^{-1}, respectively. It is, thus, evident that the saturation magnetisation value of Fe_3O_4-Mn_3O_4 NCs is lower compared to that of the Fe_3O_4NPs.[27] Inset shows the digital camera photograph of the response of the Fe_3O_4 NPs and Fe_3O_4─Mn_3O_4 NCs in the presence of a bar magnet. Strong attraction of the Fe_3O_4 NPs than that of the Fe_3O_4─Mn_3O_4 NCs towards an external magnetic field reveals that magnetism of the iron oxide particles are reduced upon conjugation with the Mn_3O_4 entities. The decrease of the saturation magnetisation can, mainly, be

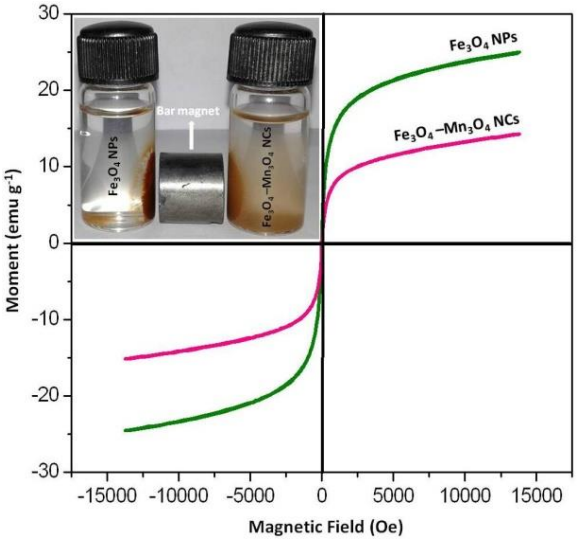

Fig. 5.7. Magnetic hysteresis curves of Fe_3O_4 NPs and Fe_3O_4─Mn_3O_4 NCs. Inset shows the digital camera photographs showing the response of the nanostructures in the presence of a magnetic bar.

attributed to the co-existence of weakly magnetic Mn_3O_4 in the composites. Therefore, the as-synthesisedFe_3O_4─Mn_3O_4 NCs with reduced magnetism may hold a great promise to be utilised as a nanoplatform for sensing of different biological species and processes.

5.1.3.8. *In-vitro* Cytotoxicity Studies on the Macrophages with Fe_3O_4–Mn_3O_4Nanocomposites

5.1.3.8.1. Isolation of Splenic Macrophages from Mice

Spleen tissue was collected from individual mice and it was homogenised in Alsever's solution using Frosted glass slide. This homogenate was poured on Histopaque1077 in 1:1 ratio and performed density gradient centrifugation. After centrifugation at 1500 rpm for 30 min, splenic macrophages were isolated from interface.

5.1.3.8.2. Cell Viability Assay

In a typical experiment, 10^6 cells were seeded in 96 well tissue culture plate and were kept overnight in CO_2 incubator. Then, the cells were treated with different concentrations of Fe_3O_4─Mn_3O_4nanocomposites (1.8×10^6– 1.8×10^{13} particles/ml) for 24 h. At the end of NCs exposure, toxicity was measured by 3-(4, 5-dimethylazol-2-yl)-2,5-diphenyl-tetrazolium bromide (MTT) assay. In control experiment, cells were followed without any NCs treatment. Then, the cell viability was measured depending on the enzymatic reduction of MTT, a yellow tertazolium salt to purple formazan at 570 nm with reference wavelength of 630 nm using microplate reader (i-Spectra plus; Bio-Rad). A schematic presentation showing the conversion of

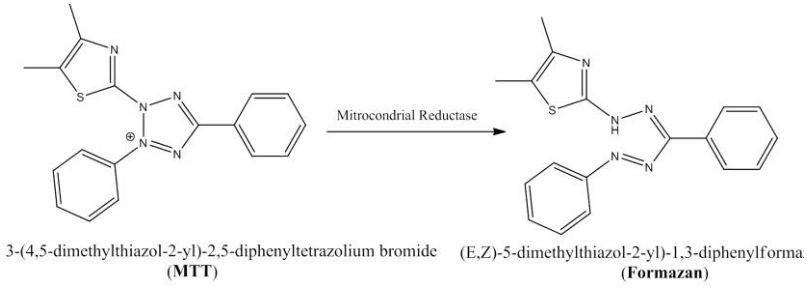

Scheme 5.2. Schematic presentation showing the conversion of MTT to formazan

MTT to formazan in the presence of microbial reductase is shown in Scheme 5.2. All the experiments have been repeated thrice and an average of three determinations has been taken. The cell viability has been shown in percentage comparison to control that

has been considered as 100%. All the raw data obtained have been followed by calculation and validated with statistical tools, such as, ANOVA, SEM, mean and variance etc. The data has been presented in mean ± SEM format and the significance has been tested at $P < 0.05$.Nitroblue tetrazolium (NBT) assay was performed in order to get the quantitative estimation of superoxide present in different test samples. The formation of formazan by the reaction of superoxide in the samples with NBT supplied in presence of EDTA catalyst gives blue color measurable in visible spectra, which indicates the amount of superoxide present in the sample and their alteration upon nanoparticle treatment. From the NBT assay, the concentration of NBT was calculated from the OD at 630nm and the extent of ROS present was determined.

5.1.3.9. Analysis of *In-vitro* Cytotoxicity Studies on the Macrophages with Fe_3O_4–Mn_3O_4 Nanocomposites

Now, the moderately magnetic Fe_3O_4–Mn_3O_4nanocomposites have been exploited to study *in-vitro* cytotoxicity in the splenic macrophages in a dose variant manner following the protocol reported in the literature.[2,3,4] The macrophages were isolated from the mice spleen and cultured in RPMI 1640 fortified with fetal calf serum. Proliferation of spleenocytes was evaluated by 3 (4, 5-dimethylthiazole-2-yl)-2, 5-diphenyltetrazolium bromide (MTT) assay and immunomodulatory activity of the extract was examined on murine macrophage phagocytosis by nitrobluetetrazolium (NBT) dye reduction, myeloperoxidase (MPO) activity and nitric oxide (NO) estimation assay. A detailed of the experimental procedure is described here. All the experiments have been repeated thrice and an average of three determinations has been taken. The cell viability has been shown in percentage comparison to control that has been considered as 100%. All the raw data obtained have been followed by calculation and validated with statistical tools, such as, ANOVA, SEM, mean and variance etc. The data has been presented in mean ± SEM format and the significance has been tested at $P < 0.05$.Fig. 5.8. shows the histograms representing the *in-vitro* cytotoxicity studies on the splenic macrophages with Fe_3O_4─Mn_3O_4 nanocomposites. A MTT assay has been used for assaying cell survival and proliferation based on the concentration of formazan generated which is directly proportional to the cell number. It is seen that the cell viability displays a concentration-dependent effect (top left panel). Nanoparticle doses, as determined by MTT assay, have been fitted in a non-linear dose response curve (as shown in the inset) and it is seen that the IC_{50}

(inhibitory concentration with 50% viability) of NCs is *ca.* 3.83×10^9 particles/ml of the solution. Therefore, for the rest of the studies, the effective concentration of the nanoparticles has been so chosen that it should fall below the value of IC_{50} and has been selected as 1.8×10^9 particles/ml of the solution.

The phagocytosis of the particles by macrophages is, usually, accompanied by a burst of oxidative metabolism allowing the generation of oxygen species which can be

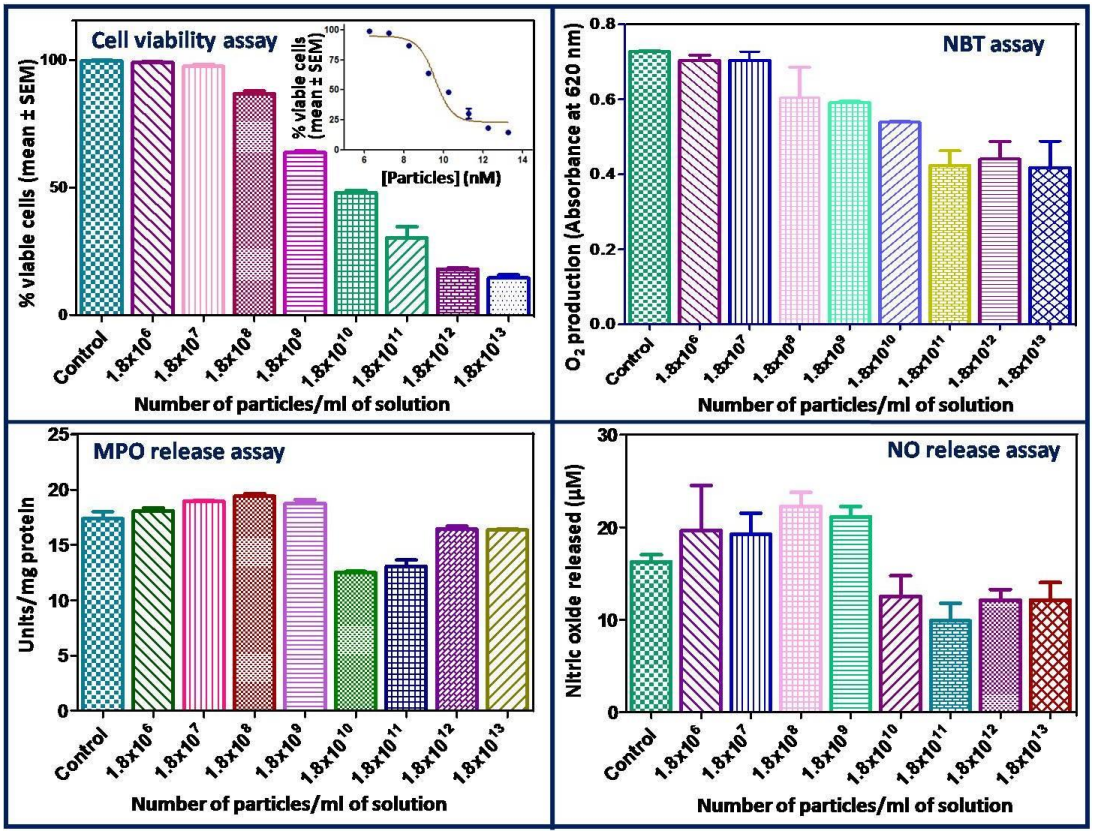

Fig. 5.8. Histograms showing the *in-vitro* cytotoxicity studies on the splenic macrophages with Fe_3O_4–Mn_3O_4 nanocomposites. Inset in the top left panel shows the determination of $IC_{50}$of the cell viability assay.

detected through reduction of nitroblue tetrazolium dye. The higher reduction in NBT assay represented higher activity of the oxidase enzyme reflecting the stimulation of phagocytes in proportion to the foreign particles ingested. The oxidative burst, as evident from the NBT reduction assay, shows a dose-dependent gradual increase (top right panel). However, the non-significant response for effective dose in NBT assay indicates that the cells are not in hypoxic condition and still maintain the normoxia which means that the cells do not experience the oxygen stress. Again, myeloperoxidase is a heme protein secreted by neutrophils and macrophages which

use the oxidizing potential of H_2O_2 to convert Cl^- into HOCl, a potent bactericidal agent. A deficiency of MPO is indicative of an autosomal recessive genetic disorder featuring deficiency, either in quantity or of function of the enzyme. It is seen that the NCs did not show any visible effect on MPO release (bottom left panel) that could be because of the indigenous Fe of the enzyme itself. The non-significant level of MPO suggested that the particles are not imposing any oxidative stress.

Lastly, nitric oxide has been found to be the main effector molecule produced by macrophages by inducible nitric oxidosynthetase (iNOS) for cytotoxic activity and can be used as a quantitative index of macrophage activation. It is seen that the NCs could determine the nitrosative stress on the splenic macrophages as revealed by the increase in NO release till 1.6×10^9 dose after which the NCs becomes cytotoxic. The significant level of NO release indicates that the particles generate reactive nitrogen species, largely, indicating the effect of NCs on the intracellular metabolic status in splenic macrophages.

5.1.5. Conclusion

In a nutshell, the integration of magnetism of multicomponent Fe_3O_4–Mn_3O_4 nanocomposites has been exploited for *in-vitro* cytotoxicity determination on splenic macrophages of mice. The present study clearly demonstrates that moderately magnetic nanocomposites could measure the oxidative and nitrosative stress of the immune competent cells. Further studies can be elicited to study the effect of these nanocomposites *in-vivo* experiments in living systems and their therapeutic potential could be adjudged.

5.2. Hybrid Mn_3O_4–NiO Nanocomposites as Electrocatalysts

5.2.1. Introduction

As a rescue to the global energy challenges, catalytic water splitting is the present state-of-the-art concept to generate clean, carbon-free, renewable energy sources and thus, to remove the energy environmental complications caused by burning fossil fuels.[28-29] The oxidation of H_2O to O_2 is the key challenge in the production of chemical fuels from electricity.[30] On the otherhand, hydrogen has been proposed as an ideal energy storage because of its high energy density and may improve the usability of renewable energy sources.[31-32] Water splitting involves two half-reactions: a reduction of water to hydrogen, and an oxidation of water to oxygen and therefore, water oxidation has become a promising research arena inspired by research challenges.[33] In natural and many other protocols for artificial photosynthesis, water oxidation, $2H_2O \rightarrow O_2 + 4H^+ + 4e^-$, is one of the most significant steps.[34-35] Plant life is bestowed upon complex catalytic systems for the dissociation of water into its elements and a critical understanding of these systems could pioneer our conceptives in the design of simpler catalysts.[36] Electrochemical water splitting has received extensive attention because this process can convert electric energy from renewable but intermittent sources into chemical energy for facile storage and delivery.[37–39] However, the overall water splitting reaction comprises of water oxidation as one of the half-reactions, which is difficult from an electrochemical point of view and thus, often, requires high overvoltage.[40] Although, several types of catalysts have, already, been developed for electrochemical water oxidation reaction[41-42] ample challenges still remain towards the eventual goal of an efficient, inexpensive and robust electrocatalysts made of cheap and earth-abundant elements. Amongst the transition metal electrocatalysts, manganese-based systems are of significant interest because of the large scale earth-abundance of manganese minerals as well as these materials mimic the role of manganese in biological water oxidation reaction in the process of Photosystem II.[43-46] A closer inspection in the series of manganese oxides available in various oxidation states of manganese (II, III, IV), hausmannite (Mn_3O_4) has been found to be an efficient and inexpensive catalyst in a number of oxidation and reduction reactions.[47,48] On the other hand, nickel oxide (NiO), is a wide band gap *p*-type semiconductor material and has attracted considerable interest due to its high

dynamic dispersion, low cost and high electrochromic efficiency.[49] The synthesis of nanocomposites containing two or more disparate functionalities have been of significant interest due to their altered and/or enhanced physicochemical properties.[50,51]

In this sub-section, we have explored the controllable integration into Mn_3O_4–NiO nanocomposites by seed-mediated epitaxial growth of NiO from nickel precursor on the surface of preformed poly (vinylpyrolidone)-stabilised Mn_3O_4 nanoparticles. The as-synthesised nanostructures have been characterised by absorption spectroscopy, transmission electron microscopy, high resolution transmission electron microscopy, selected area electron diffraction pattern, scanning electron microscopy, energy dispersive X-ray spectroscopy, elemental mapping, Fourier transform infrared spectroscopy, X-ray diffraction technique and thermogravimetric analysis. Then, the electrocatalytic activity of these combinatorial catalysts towards water oxidation reaction has been investigated in the presence of sunlight and ultraviolet light at low overpotential and under neutral pH condition.

5.2.2. Experimental

5.2.2.1. Synthesis of Mn_3O_4 Nanoparticles

An aliquot of 25 mL aqueous ethanolic solution containing a mixture of $Mn(ac)_2{\cdot}4H_2O$ (2.5 mM) and PVP (0.1 M) was brought to reflux (*ca.* 65 °C) under stirring. After about 30 min, 150 µL of NH_4OH was added dropwise and the colour of the solution changes from brownish yellowish from the parent colourless solution. The refluxing was continued for overall 2 h for the development of the particles.

5.2.2.2. Synthesis of NiO—Mn_3O_4 Nanocomposites

In a typical synthesis, 25 mL aqueous ethanolic solution of $NiCl_2.6H_2O$ (2.5 mM) was brought to reflux (*ca.* 65 °C) under stirring. After about 30 min, 150 µL of NH_4OH was added dropwise continuing 1 min and immediately after, 1.0 mL of preformed Mn_3O_4 nanoparticles (0.25 mM) was

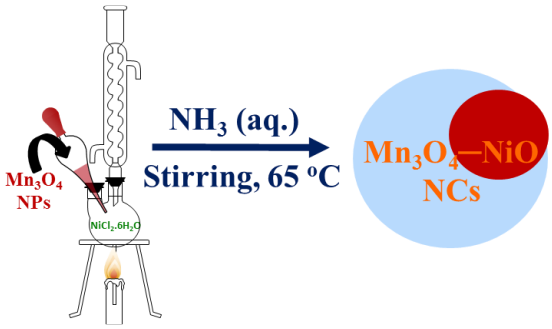

Scheme 5.3. Schematic presentation for the synthesis of Mn_3O_4–NiO nanocomposites

added dropwise continuing 10 min to the solution under reflux. The refluxing was continued for overall 1.5 h. After addition of the Mn_3O_4 colloidal dispersion, the colour of the sol was, slowly, begun to change from deep greenish yellow and finally, a yellowish green colouration was seen at the end of the reaction. Then, the heating was stopped and the mixture was stirred for 12 h at room temperature. The particles so obtained were retrieved by centrifugation at 10,000 rpm for 15 min and were, subsequently, redispersed into water. The dispersion was found to be stable for a month while stored in the vacuum desiccator.

5.2.3. Results and Discussion

An aliquot of Mn_3O_4-NiO nanocomposites has been synthesised by one-pot hydrothermal procedure by injection of preformed poly(vinylpyrolidone) (PVP)-stabilised Mn_3O_4 nanoparticles during the epitaxial growth of NiO from nickel precursor. To the best of our knowledge, this is the first report of the synthesis of Mn_3O_4-NiO nanocomposites. The as-synthesised nanostructures have been characterised by absorption spectroscopy, transmission electron microscopy, high resolution transmission electron microscopy, selected area electron diffraction pattern, scanning electron microscopy, energy dispersive X-ray spectroscopy, elemental mapping, Fourier transform infrared spectroscopy, X-ray diffraction technique and thermogravimetric analysis.

5.2.3.1. Absorption Spectra of Mn_3O_4 Nanoparticles and Mn_3O_4–NiO Nanocomposites

The absorption spectral features and determination of the band gap of Mn_3O_4 nanoparticles and Mn_3O_4–NiO nanocomposites are shown in Fig. 5.9. Panel a shows the absorption spectra of Mn_3O_4 NPs and Mn_3O_4–NiO NCs measured in the solid state. The color change of Mn_3O_4–NiO nanocomposites is clearly seen before and after Mn_3O_4 conjugation. The original color of Mn_3O_4 particles is yellowish brown and that of NiO is greenish white, while the resulting Mn_3O_4–NiO nanocomposites are whitish brown. This suggests that the finally formed Mn_3O_4–NiO nanocomposites have inherited the colorimetric character of Mn_3O_4 nanoparticles. The electronic absorption spectrum of Mn_3O_4 shows three well-defined regions: the first portion from 250 to 310 nm, the second from 310 to 500 nm (with a maximum at 325 nm), and the third one finishing at 800 nm. The first portion is assigned to the allowed $O^{2-} \rightarrow Mn^{2+}$ and $O^{2-} \rightarrow Mn^{3+}$ charge-transfer transitions, and the last two can be

reasonably related to d-d crystal-field transitions, $^3E_g(G) \leftarrow {}^3T_{1g}$, $^3A_{2g}(F) \leftarrow {}^3T_{1g}$, $^3A_{2g}(G) \leftarrow {}^3T_{1g}$, $^3T_{2g}(H) \leftarrow {}^3T_{1g}$, $^3T_{1g}(H) \leftarrow {}^3T_{1g}$, and $^3E_g(H) \leftarrow {}^3T_{1g}$, on octahedral Mn^{3+} species.[52] Upon addition of nickel precursor and subsequent hydrolysis, the absorption spectrum of Mn_3O_4 becomes perturbed indicating electronic interaction between the components in maneuvering the nanocomposites In addition, the appearance of a hump at around 325 nm could be ascribed to the band gap transition of NiO species in the composites.[53] The direct band gap energy (E_g) of the Mn_3O_4 NPs and Mn_3O_4–NiO NCs could be determined by fitting the absorption data to the direct band gap transition equation as[54]

$$(\alpha h\nu)^2 = A(h\nu - E_g) \qquad (5.1.)$$

where, α is the absorption co-efficient, $h\nu$ the photon energy and A a constant. The absorption coefficient (α) is defined as: $\alpha = 2.303\ A/L\ c$, where, A is the absorbance of

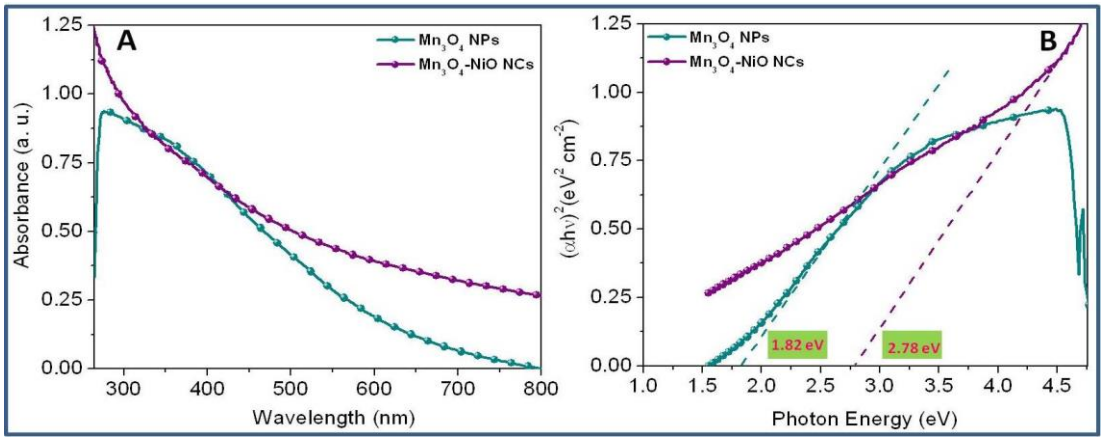

Fig. 5.9. (A) Solid state absorption spectra and (B) plot of $(\alpha h\nu)^2$ as a function of hν of Mn_3O_4 NPs and Mn_3O_4–NiO NCs.

the sample, c the loading of sample (g L^{-1}), L the path length (= 1 cm). From the profiles (panel b) showing the plot of $(\alpha h\nu)^2$ as a function of $h\nu$, the estimated direct band gap of the Mn_3O_4 NPs and Mn_3O_4–NiO NCs is *ca.* 1.82 and 2.78 eV, respectively; these results show that the band gap of Mn_3O_4–NiO NCs is in-between free Mn_3O_4 and bulk NiO (4.0 eV).[55] The reduction in the band gap authenticates the interaction between the individual species in the composites.

5.2.3.2. Fourier Transform Infrared Spectra of Mn_3O_4 NPs and Mn_3O_4–NiO NCs

Fourier transform infrared spectrum of Mn_3O_4–NiO NCs is shown Fig. 5.10. The sample was heated at 800 ^{0}C in argon atmosphere for 1 h prior to measurement. The doublet of peaks at 435 and 490 cm^{-1} could be assigned to Ni–O and Mn–O stretching

vibrations, respectively.[56] The appearance of an additional band at 860 cm^{-1} is related to the stretching vibration of Mn–O–Mn species.[57] Moreover, the presence of bands at 1406 and 1938 cm^{-1} could be attributed to the asymmetric and symmetric COO^{-} stretching vibrations of acetate chemisorption, respectively, which, probably, accounts for colloid stabilization. The broad band at 3180 cm^{-1} arise due to the stretching mode of O–H groups that reveals the existence of a small amount of water chemisorbed and/or physisorbed by the nanocomposites.[58]

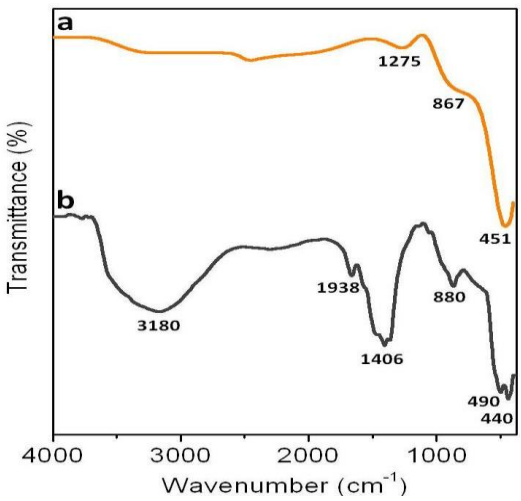

Fig. 5.10. Fourier transform infrared spectra of the (a) Mn_3O_4 NPs and (b) Mn_3O_4–NiO NCs.

5.2.3.3. Morphology, Composition and Crystallinity of the Mn_3O_4 NPs and Mn_3O_4-NiO NCs

The morphology, composition and crystallinity of the Mn_3O_4 and Mn_3O_4-NiO nanostructures are described in Fig. 5.11. Representative transmission electron

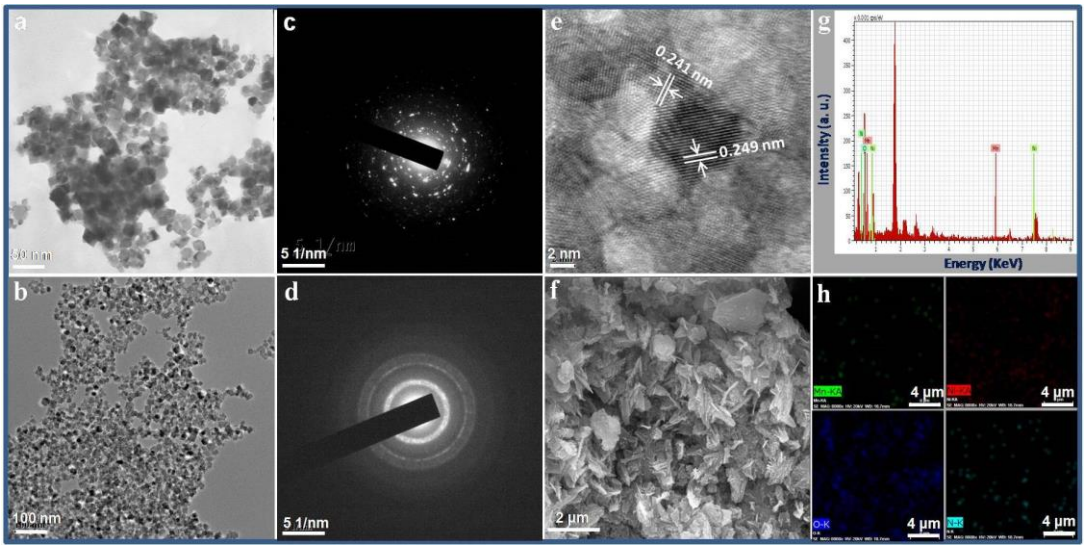

Fig. 5.11. (a, b) Representative transmission electron micrographs and (c, d) selected area electron diffraction patterns of Mn_3O_4 nanoparticles and Mn_3O_4–NiO nanocomposites, respectively; (e) high resolution transmission electron micrograph (f) scanning electron micrograph, (g) energy dispersive X-ray spectrum and (h) elemental mapping of Mn_3O_4–NiO nanocomposites.

micrograph of Mn_3O_4 (panel a) and Mn_3O_4─NiO (panel b) shows that the particles are tetragonal with average diameter 20±5 and 15±3 nm, respectively. Selected area electron diffraction pattern of the Mn_3O_4 particles (panel c) is consistent with tetragonal Mn_3O_4 with strong ring patterns due to (101), (103) and (220) planes and therefore, confirms the crystallinity of the particles.[59] Selected area electron diffraction pattern of the Mn_3O_4─NiO nanocomposites (panel d) is consistent with tetragonal hausmannite with strong ring patterns due to (101), (103) and (220) planes and also for ring pattern of (111) plane of cubic nickel oxide.[60] The observation of distinct ring patterns in the nanocomposites implies that the presence of preformed hausmannite favours the formation of an ordered and single phase of NiO in the nanocomposites.[60] High resolution transmission electron micrograph (panel e) displaying the distinct interplanar distance between the fringes is about 0.249 nm which corresponds to the distance between the (211) planes of the Mn_3O_4 tetragonal crystal lattice[61] and 0.241 nm that could be assigned to the (111) planes of NiO.[62] Scanning electron micrograph of the Mn_3O_4–NiO nanocomposites (panel f) shows that the samples exhibit large flower-like morphology which is, possibly, arising due to soft agglomerations upon drying of the magnetic particles onto the silicon wafer.[63] Representative energy dispersive X-ray spectrum of Mn_3O_4─NiO nanocomposites (panel g) reveals that the particles are composed of Mn, Ni, O and N elements; the appearance of nitrogen is from the stabilising PVP molecules. Elemental mapping of the nanocomposites (panel h) exhibits the appearance of red, green, deep blue and light blue coloured micrographs revealing the presence of nickel (Ni), manganese (Mn), oxygen (O) and nitrogen (N), respectively

5.2.3.4. X-ray Diffraction Pattern of Mn_3O_4 NPs and Mn_3O_4–NiO Nanocomposites

For structural characterization of synthesized materials, a comparative X-ray diffraction pattern of Mn_3O_4 NPs and Mn_3O_4–NiO nanocomposites is shown in Fig.5.12. Trace a is of the manganese oxide nanoparticles; all diffraction

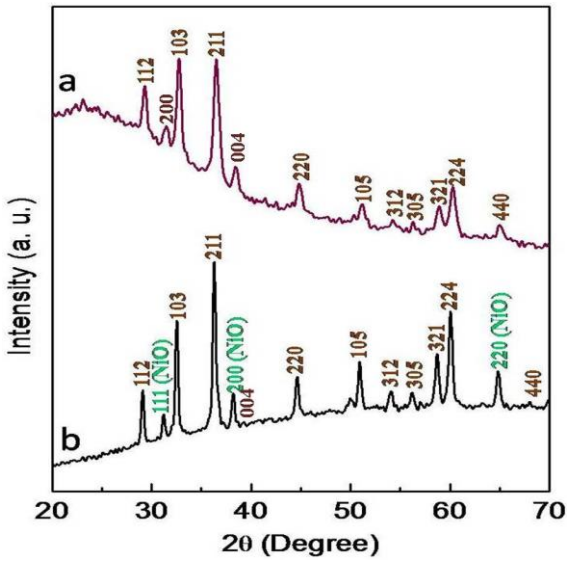

Fig. 5.12 X-ray diffraction patterns of (a) Mn_3O_4 NPs and (b) Mn_3O_4–NiO NCs.

peaks implying a crystalline structure can be indexed to the tetragonal hausmannite structure with lattice parameters, a = b = 5.762 Å, and c = 9.469 Å and space group $I4_{I/amd}$, which are consistent with the standard values of bulk Mn_3O_4 (JCPDS# 24-0734)[64]. Trace b represents the X-ray diffraction pattern of NiO-Mn_3O_4 NCs. The presence of all the diffraction peaks implying a crystalline structure that can be indexed to the tetragonal hausmannite structure of Mn_3O_4 (JCPDS# 24-0734) and cubic phase of nickel oxide (JCPDS# 47-1049) with space groups $I4_{I/amd}$ and Fm3m, respectively, which indicates that preformed hausmannite favours the formation of an ordered and single phase of NiO in the nanocomposites.[65]

5.2.3.5. Thermogravimetric Analysis of Mn_3O_4–NiO Nanocomposites

Thermogravimetric analysis (Fig. 5.13) of the as-dried powder sample shows two weight loss steps in the curve: 2.0 wt% loss corresponding to the water desorption (up to 200 °C), and a weight loss of 4.5 wt % over 200–800 ºC as a result of the decomposition of the PVP polymer, verifying that the polymer molecules are, indeed, incorporated into the nanocomposites.[66]

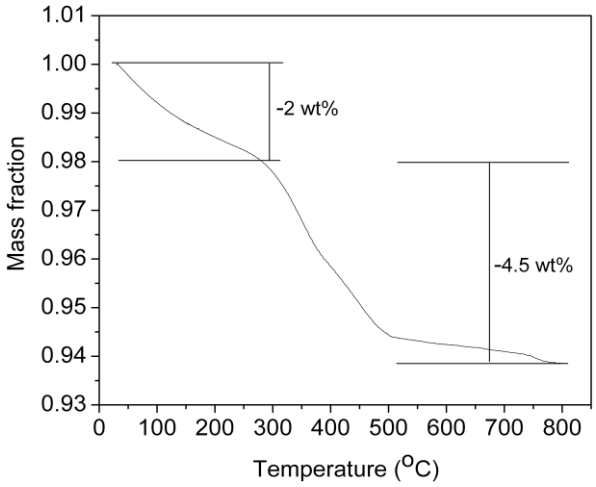

Fig. 5.13. TGA weight loss pattern of the as-synthesised Mn_3O_4–NiO NCs.

5.2.3.6. Electrode Modification and Characterisation

A mechanically and electrochemically cleaned gold electrode (2 mm in diameter) was immersed into an undisturbed colloidal dispersion of PVP-stabilised Mn_3O_4–NiO nanocomposites. After 6 h, a Mn_3O_4–

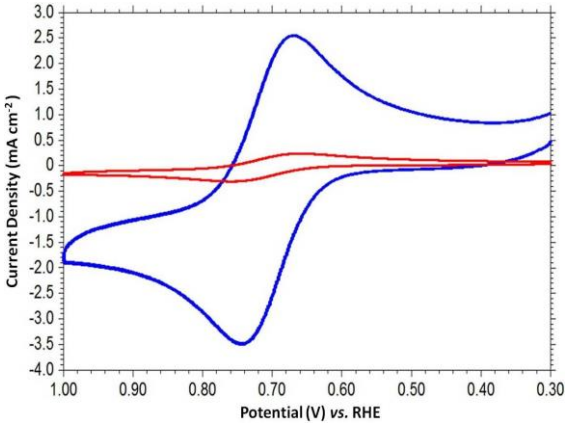

Fig. 5.14. Overlaid cyclic voltammogram of 0.5 mM $[Fe(CN)_6]^{4-}$ in 0.1 M PBS at pH~7.0 using bare (red) and Mn_3O_4–NiO modified (blue) gold electrode.

NiO layer was formed over the gold electrode. The modified working electrode Mn_3O_4–NiO–Au was washed thoroughly with double distilled water and dried in nitrogen atmosphere for further use. The modification of the gold electrode with the NCs (Fig. 5.14) has been confirmed by cyclic voltammetry (CV) and electrochemical impedance spectroscopy (EIS) using the redox probe $[Fe(CN)_6]^{3-/4-}$ in 0.1 M PBS at pH~7.0. The cyclic voltammogram of 0.05 mM $[Fe(CN)_6]^{4-}$ exhibits an irreversible redox couple at bare electrode. After modification of the gold electrode with Mn_3O_4–NiO NCs, a quasireversible couple (ΔE = 70 mV) with large current height has been obtained which is indicative of the better electronic communication between the probe and gold electrode through Mn_3O_4–NiO layer. Electrochemical impedance spectroscopy of bare and Mn_3O_4–NiO modified gold electrode is shown in Fig. 5.15. The surface coverage (θ =0.92) has been obtained by using the equation, $\theta = [1-(i_p/i_p^o)]$, where, i_p (0.21 mA cm^{-2}) and i_p^o (2.58 mA cm^{-2}) are peak currents of the redox probe at bare and Mn_3O_4–NiO modified gold electrodes, respectively, under similar conditions. Therefore, electrochemical impedance spectroscopic analysis supports and supplements the observations through cyclic voltammetry.

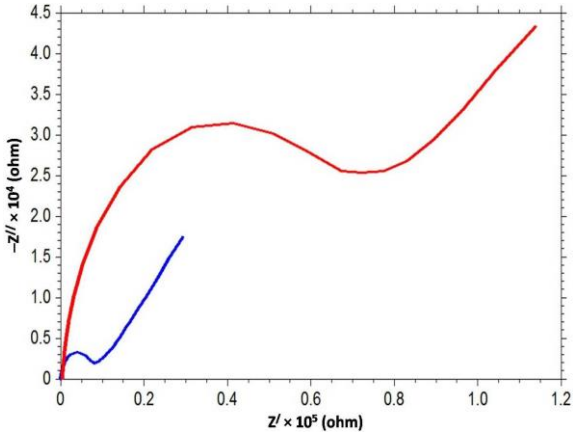

Fig. 5.15. Overlaid Nyquist plot (-$Z^{//}$ *versus* $Z^{/}$) of 0.5 mM $[Fe(CN)_6]^{4-}$ in 0.1 M PBS at pH~7.0 using bare (red) and Mn_3O_4–NiO modified (blue) gold electrodes.

5.2.3.7. Overlaid Cyclicvoltammogram of Mn_3O_4 and Mn_3O_4–NiO Modified Gold Electrodes in 0.1 M PBS at pH~7.0

The overlaid cyclic

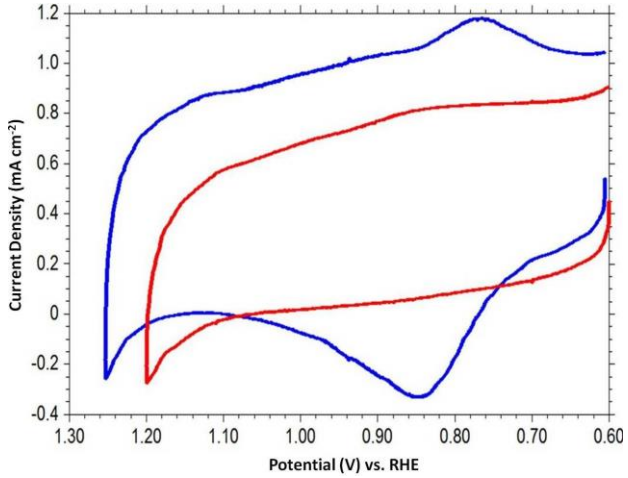

Fig. 5.16. Overlaid cyclicvoltammogram of Mn_3O_4 (red) and Mn_3O_4–NiO (blue) modified gold electrodes in 0.1 M PBS at pH~7.0.

voltammogram of Mn_3O_4 and Mn_3O_4–NiO modified gold electrode is shown in Fig. 5.16. After modification with Mn_3O_4 NPs, there is no appearance of prominent oxidation or reduction peaks, while after with Mn_3O_4–NiO NCs, an oxidation peak is seen near 0.84 V due to NiO oxidation and corresponding reduction peak at 0.78 V.[50] These results prove the proper modification of the electrodes with the nanostructures.

5.2.3.8. Comparative Linear Sweep Voltammograms (LSV) of Electrocatalytic Oxidation of Water

The electrocatalytic activity of Mn_3O_4–NiO nanocomposites towards water oxidation has been examined by measuring comparable linear sweep voltammograms (LSV) at bare, Mn_3O_4 and Mn_3O_4–NiO modified gold electrodes in 0.1 M PBS at neutral pH (Fig. 5.17). It is seen that the anodic peak potential shifted towards less positive potential with a large increase of current (J = 2.3 mA cm^{-2}) at Mn_3O_4–NiO modified gold electrode compared to bare and Mn_3O_4-modified gold electrodes. These results suggest that the Mn_3O_4-NiO modified gold electrode electrocatalytically

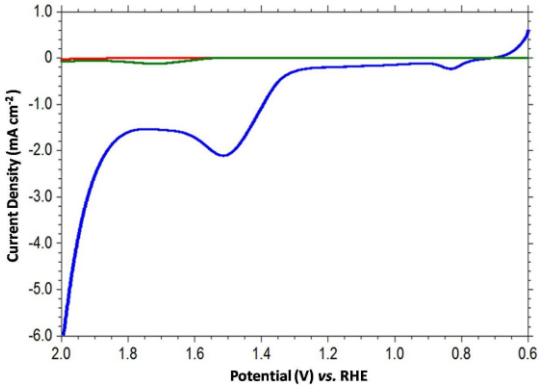

Fig. 5.17. Overlaid linear sweep voltammograms obtained from 0.1 M PBS (pH~7.0) at bare Au (red), Mn_3O_4–Au (green) and Mn_3O_4–NiO–Au (blue) electrodes.

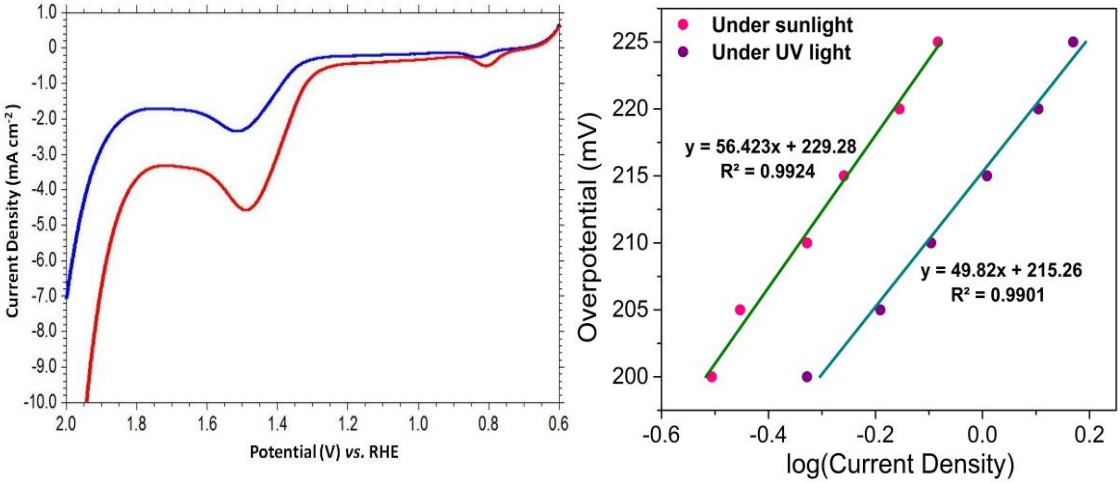

Fig. 5.18. (left) Overlaid linear sweep voltammograms obtained at Mn_3O_4–NiO–Au electrode in 0.1 M PBS (pH~7.0) in the presence of sunlight (blue) and UV light (red). (right) Tafel plot of electrocatalytic oxidation of water with Mn_3O_4–NiO–Au electrode in 0.1 M PBS (pH~7.0) at different applied potentials in the presence of sunlight and UV light.

oxidised water with an overpotential of η≈ 280 mV at pH ~7.0. Fig. 5.18 shows the overlaid linear sweep voltammograms obtained at Mn_3O_4–NiO–Au electrode in 0.1 M PBS (pH~7.0) in the presence of sunlight and UV-light. It is seen that, in presence of UV light, the anodic peak current is shifted towards the more negative potential (~ 0.05 V) and current density increases by 2.2 mA cm^{-2} under the experimental condition. The Tafel plot of overpotential (η) *versus* log J (where, J is current density) with Mn_3O_4–NiO–Au modified electrode for electrocatalytic oxidation of water produces slope of ~56 and ~ 50 mV per decade in the presence of sunlight and UV light, respectively, which indicates that the catalytic activity increases in the presence of ultraviolet light.

5.2.3.9. Electrocatalytic Oxidation of Water at Mn_3O_4–NiO–Au Electrode in Acetate Buffer Solution

The electrocatalytic oxidation of water has also been tried in 0.1 M acetate buffer medium (pH ~ 7.0); interestingly, similar response has been observed in acetate buffer medium (Fig.5.19). Moreover, it was also noted that no such oxidation peak could be observed at Mn_3O_4–NiO–Au electrode in non-aqueous media, like, acetonitrile (CH_3CN) or dichloromethane (CH_2Cl_2) etc. which indicates that the evolution of oxygen occurs from the oxidation of water. In addition, upon addition of water in acetonitrile solvent (containing 0.1 M $[Bu_4N][ClO_4]$, pH~7.0), an oxidative peak appears at ~ +1.5 V. These observations points out that the evolution of oxygen from water oxidation in the presence of nanocomposites are not restricted to the presence of phosphate buffer saline only; it can happen in buffer media with desired pH.

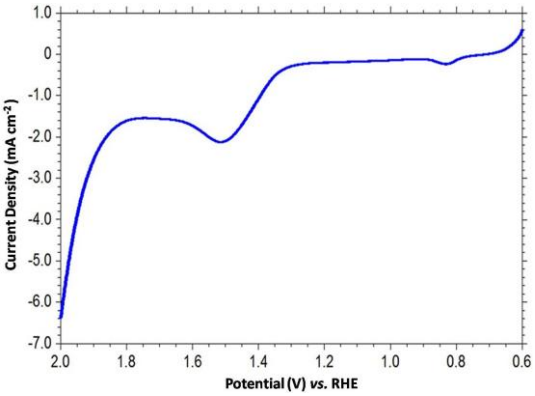

Fig. 5.19. Linear sweep voltammogram obtained at Mn_3O_4–NiO–Au electrode at 0.1 M acetate buffer solution (pH~7.0)

5.2.3.10. Electrocatalytic Oxidation of Water at Mn_3O_4–NiO–Au Electrode with Different Water Concentrations

Fig.5.20 shows the linear sweep voltammograms obtained from Mn_3O_4–NiO–Au electrode with increasing water concentration (0.1 to 1.0 M). It is seen that the Mn_3O_4–NiO–Au electrode displays an anodic response at + 1.5 V *versus* RHE in 0.1 M PBS at pH~7.0, signifying water oxidation, $2H_2O \rightarrow O_2 + 4H^+ + 4e^-$. A profile showing the plot of anodic peak current density *versus* [H_2O] is shown in the inset. It is noted that, initially, the anodic peak current density increases with increasing water concentration (up to 0.6 M) and thereafter, the current density remains constant, as expected for surface-attached composite materials[35] and confirms that O_2 is generated, solely, due to water oxidation.

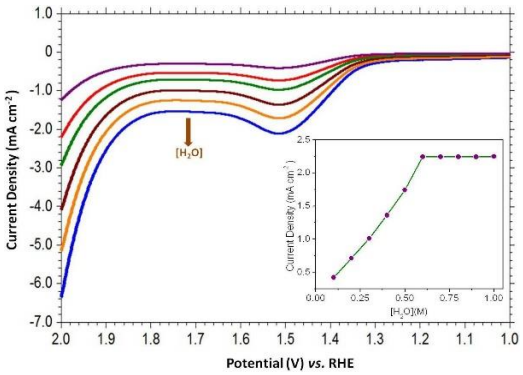

Fig. 5.20. LSV obtained from Mn_3O_4–NiO–Au electrode with increasing [H_2O] (0.1 to 1.0 M). Inset shows a plot of anodic peak current density *versus* [H_2O].

5.2.3.11. Electrocatalytic Oxidation of Water at Mn_3O_4–NiO–Au Electrode with Different Scan Rates

The linear sweep voltammogram (Fig. 5.21) for the oxidation of water obtained with Mn_3O_4–NiO–Au electrode at 0.1 M PBS (pH~7.0) has been measured at different scan rates. It is seen that the oxidation peak current increases with the scan rate in the range of 50–100 mV s^{-1} and follows the linear regression equation (as shown in the inset), J (mA cm^{-2}) = 0.0136 V + 1.0629 (R^2 = 0.9984), which confirms that the electro-oxidation of water at the Mn_3O_4–NiO modified electrode is a surface-controlled process.[67]

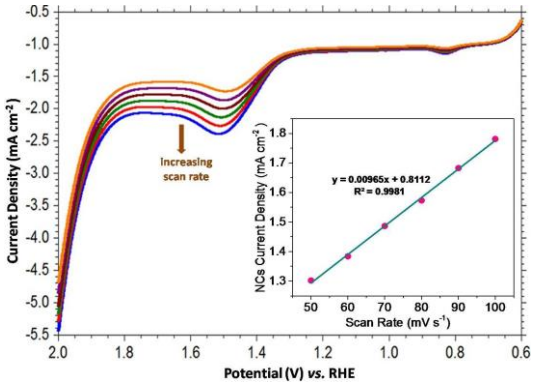

Fig. 5.21. Linear sweep voltammogram obtained with Mn_3O_4–NiO–Au electrode in 0.1 M PBS (pH~7.0) at different scan rates. A plot of current density of the nanocomposites as a function of scan rate is shown in the inset.

5.2.3.12. Profile Showing the Variation of Anodic Peak Potential as a Function of lnν The number of electrons involved in the water oxidation process, could be calculated from Laviron equation[68] $E_{pa} = E^o + RT/(1-\alpha)nF[\ln\{RTk_s/(1-\alpha)nF\} + \ln\nu]$, where, E° is the standard potential, E_{pa} the anodic peak potential, α the anodic electron transfer coefficient, n the number of electrons, k_s the rate of electron transfer, ν the scan rate and R, T and F have their usual significance. A profile (Fig. 5.22) showing the variation of anodic peak potential as a function of lnν, where, ν is the scan rate shows the linear relationship as, $E_{pa} = 1.374 + 0.0297 \ln\nu$, $R^2 = 0.996$. While the slope of the curve, RT/(1-α)nF is estimated as 0.0297 and considering, α = 0.5 for an absolute irreversible electron transfer (as evident from cyclic voltammetry measurements), the number of electrons, n ≈ 3.97 which is close to the expected value of n = 4, since four electrons are involved in the oxidation of two water molecules, coupled with the removal of four protons to form a new O−O bond in this endo-thermic transformation.[69,70]

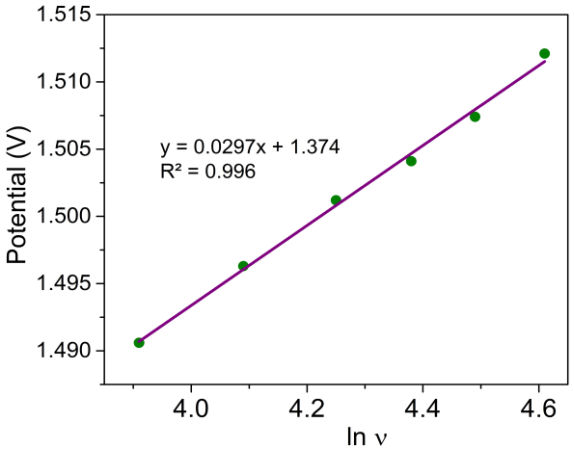

Fig. 5.22. Profile showing the variation of anodic peak potential as a function of lnν.

5.2.3.13. Cyclic Voltammogram of 0.1 M PBS (pH~7.0) at Mn_3O_4–NiO–Au Electrode

A cyclic voltammogram of 0.1 M PBS (pH~7.0) at Mn_3O_4–NiO–Au electrode is shown in Fig. 5.23. Now, the effect of pH on the electrocatalytic oxidation of water at Mn_3O_4–NiO–Au electrode has been studied in the range of 5.0 – 9.0 of PBS at a scan rate of 100 mV s^{-1}. It is seen that the anodic peak potential is shifted towards more negative value with increasing pH of the medium.

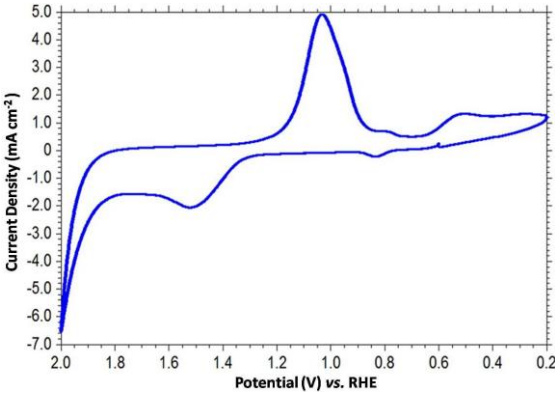

Fig. 5.23. Cyclic voltammogram of 0.1 M PBS (pH~7.0) at Mn_3O_4–NiO–Au electrode.

5.2.3.14. Electrocatalytic Oxidation of Water at Mn_3O_4–NiO–Au Electrode at Different pH

The effect of pH on the electrocatalytic oxidation of water at Mn_3O_4–NiO–Au electrode has been studied in the pH range of 5.0 – 9.0. Fig.5.24 illustrates the linear sweep voltammogram at varying pH values of PBS at Mn_3O_4–NiO–Au electrode. It is seen that the anodic peak potential is shifted towards the more negative potential with increasing pH of the medium. The oxidation peak potential varies linearly with increasing pH and follows the linear regression equation, E_{pa} = -0.059 pH + 1.927, R^2 = 0.9968 (as shown in the inset). The slope of 59 mV per pH unit indicates that equal number of protons and electrons are involved in the electrode reaction process.[68]

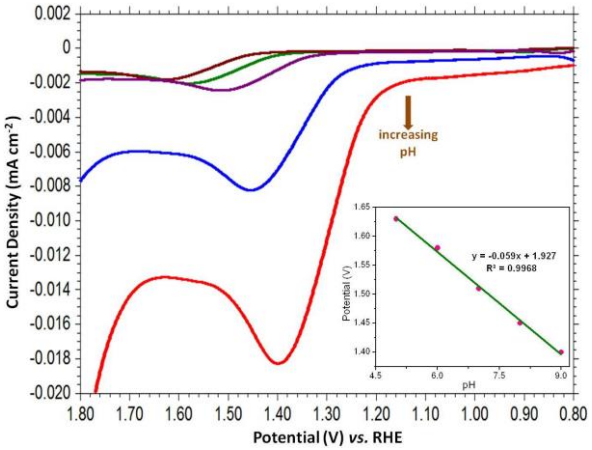

Fig. 5.24. Overlaid linear sweep voltammogram derived from Mn_3O_4–NiO–Au electrode at different pH of 0.1 M PBS (5.0, brown; 6.0 green; 7.0, violet, 8.0, blue and 9.0, red) at a scan rate of 100 mV s^{-1}. Inset shows the plot of oxidation peak potential as a function of pH.

5.2.3.15. Oxygen Evolution Curve During Electrocatalytic Oxidation of Water with Mn_3O_4–NiO Modified Electrode under Neutral pH Condition and Digital Camera Photograph Showing the Bubbling of Oxygen on the Electrode Surface

A digital photograph showing the evolution of gas bubbles during the electrocatalytic oxidation of water on Mn_3O_4–NiO modified electrode surface is shown in Fig. 5.25. The amount of oxygen formed during the electrolysis has measured using fluorescent probe technique. During the electrolysis of water, the amount of dissolved O_2 in the solution increases from *ca.* 30 – 170 μM with a Faradic efficiency (= amount of O_2 × number of electrons needed to produce O_2/amount of charge passed to the solution) of around 90%. The Faradic efficiency for the O_2 evolution increases by ~6 % in presence of UV light (ESI 15). On the basis of steady state measurements, the apparent turnover frequency (TOF) is *ca.* 5.1 s^{-1} (I = 2.31 mA cm^{-2}, Q = 0.53 mC

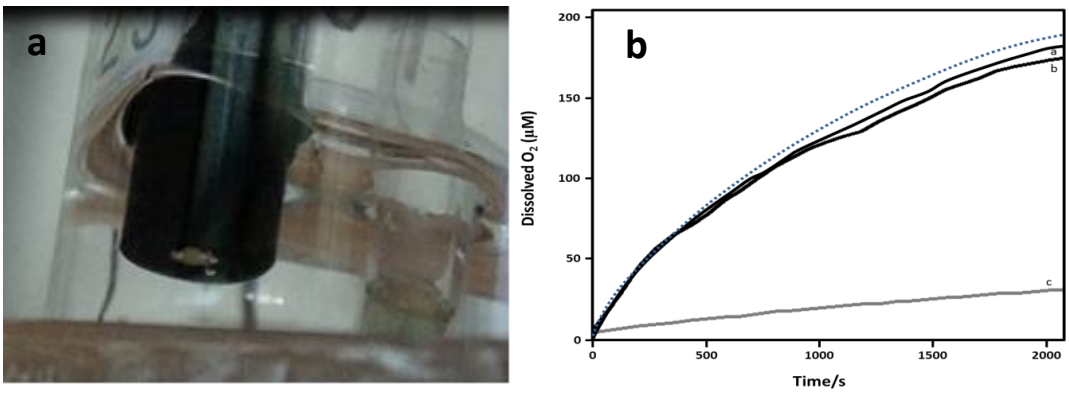

Fig. 5.25 (a) Digital photograph showing the bubbling of oxygen on the electrode surface, (b) Oxygen evolution during the controlled potential electrolysis of water in a gas-tight electrochemical cell containing 0.1 M PBS (pH~7.0) at bare Au (curve c) and Mn_3O_4–NiO–Au electrodes in the presence of sunlight (curve b) and ultraviolet light (curve a) as measured with a fluorescence probe. Dotted line represents the theoretical oxygen evolution with 100% efficiency.

cm^{-2}) in the presence of UV light which is higher than that obtained under ambient condition (4.3 s^{-1}).

5.2.3.16. Controlled Potential Electrolysis (CPE) of Mn_3O_4–NiO Modified Gold Electrode

Controlled potential electrolysis (CPE) in the presence of sunlight and UV light shows constancy of current density with time which indicates high stability of the Mn_3O_4–NiO modified gold electrode during the electrolysis. Chronopotentiometry at Mn_3O_4–NiO–Au electrode in 0.1 M PBS (for 30 min at 2.5 mA cm^{-2}) also supports the good stability of the electrode during electrolysis of water (Fig. 5.26.).

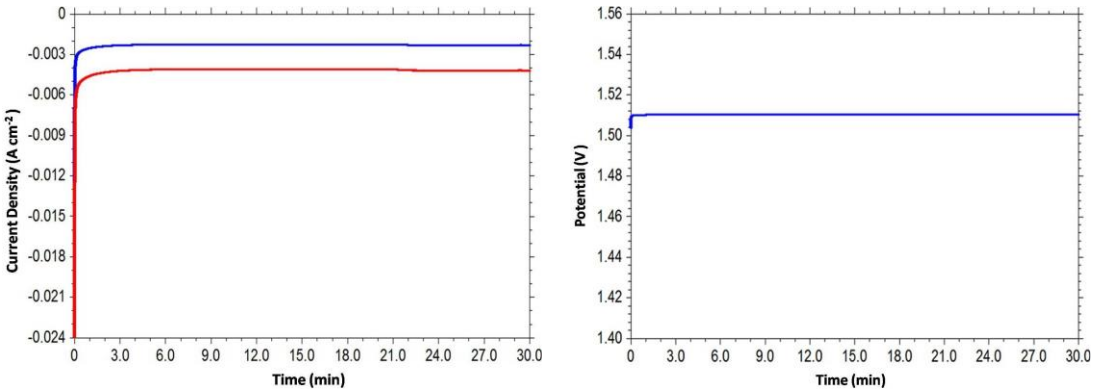

Fig. 5.26. (left) Controlled potential electrolysis with Mn_3O_4–NiO modified electrode in 0.1 M PBS (pH~7.0) at +1.5 V *versus* RHE in the presence of sunlight (blue) and UV light (red); (right) chronopotentiogram with Mn_3O_4–NiO modified electrode in 0.1 M PBS (pH~7.0) at 2.5 mA cm^{-2}.

5.2.3.17. Long-term Stability of Mn_3O_4–NiO Modified Electrode Under Neutral pH Condition

Fig. 5.27 shows the long-term stability of the Mn_3O_4–NiO modified electrode was explored by LSV measurement in 0.1 M PBS over 15 days time span (for storing purpose, a rubber cap was used to cover the modified electrode surface), and almost similar LSV responses were obtained after 3, 6, 10 and 15 days (relative standard deviation is 0.04%).

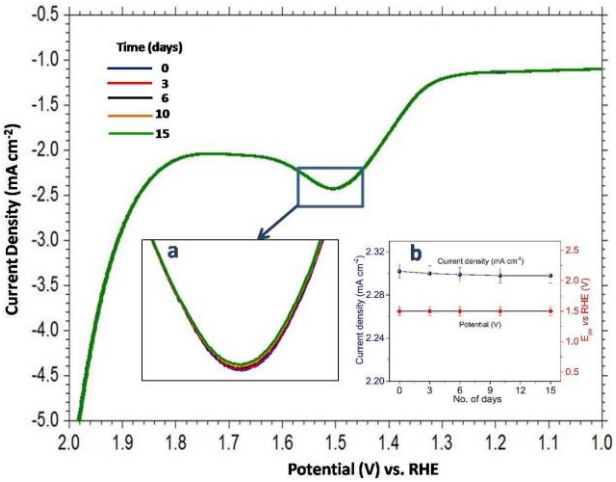

Fig. 5.27. Overlaid linear sweep voltammograms obtained at Mn_3O_4–NiO–Au electrode in 0.1 M PBS (pH~7.0) at different time intervals. Insets show (a) the enlarged view and (b) plot of anodic peak current and anodic peak potential *vs.* time.

5.2.3.18. A Comparative Account of the Performances of Some Related Electrocatalysts for Water Oxidation Reaction

A comparative account of some related electrocatalysts reported in the literature and the present method for the electrocatalytic oxidation of water is presented in Table 5.1. It can be observed that the overpotential, current density and turnover frequency of the present method are comparable or in some cases better than the methods reported in the literature; this highlights the usability of the present method in water oxidation reaction.

Table 5.1. Comparison of the Performances of Some Related Electrocatalysts for Water Oxidation Reaction

Catalysts	Overpotential (mV)	Current density (mA cm^{-2})	TOF (s^{-1})	pH	Reference
Manganese oxides (MnO_x)	0.57	1.0	1.05×10^{-3}	5.8	Suib et al., *ACS Catal*., 2015, **5**, 1693−1699.
α-MnO_2-Py nanoparticles	0.66	1.0	3.1×10^{-3}	7.5	Nakamura et al., *Nat. Commun.*, 2014, **5**, 4256 1−6.
MnOx thin flims	0.45	1.0	–	7.0	Fiechter et al., *J. Phys. Chem. C*, 2014, **118**, 14073–14081.
NiOx-en (FTO)	0.51	1.0	0.02	9.2	Brudvig et al., *J. Am. Chem. Soc.*, 2001, **123**, 423–430.
Mesoporous IrOx film	0.29	0.5	4.1	13.0	Murray et al., *J. Phys. Chem. C*, 2009, **113**, 12959–12961.
$NiCo_2O_4$ nanoparticles	0.56	1.0	–	13.0	Zhao et al., *J. Phys. Chem. C*, 2014, **118**, 25939–25946.
Au-Mn_3O_4 NCs	0.37	–	4.6	7.5	Ghosh et al., *RSC Adv.*, 2014, **4**, 41976–41981.
Mn_3O_4–NiO NCs	0.28	2.2 4.5 (UV)	4.3 5.1 (UV)	7.0	Present Work

5.2.4. Conclusion

In conclusion, manganese oxide–nickel oxide nanocomposites synthesised by seed-mediated epitaxial growth could overcome the key challenges at the present state-of-the-art research of electrocatalytic water oxidation, surprisingly, at a neutral pH (pH~7.0) and a low overpotential of 280 mV, which is beyond the typical range of many homogeneous water oxidation catalysts (600–900 mV). Moreover, the turnover frequency (*ca.* 4.3 s^{-1}) and Faradic efficiency (~90%) for the O_2 evolution are very high and increases in presence of UV light in comparison with the ambient condition. As manganese oxides are available in various oxidation states and exhibit extensive biomimetic chemistry with oxygen, combinatorial catalysts with nickel oxide illuminates ample opportunities in water oxidation electrocatalysis using a wide variety of inexpensive and earth-abundant materials.

5.3. References

1. M. De, P. S. Ghosh and V. M. Rotello, *Adv. Mater.*, 2008, **20**, 4225─4241.
2. A. K. Abbas, A. H. H. Lichtman and S. Pillai, In *Basic Immunology: Functions and Disorders of the Immune System*, 4th edn., Saunders, Wilmington, USA, 2012.
3. J. Sun, A. Siroy, R. K. Lokareddy, A. Speer, K. S. Doornbos, G. Cingolani and M. Niederweis, *Nature Struct. Mol. Biol.*, 2015, **22**, 672─678.
4. G. W. Cox, Assay for Macrophage-Mediated Anti-Tumor Cytotoxicity In *Current Protocols in Immunology*, John Wiley and Sons, New York, 2003.
5. J. Gao, H. Gu and B. Xu, *Acc. Chem. Res.*, 2009, **42**, 1097─1107.
6. S. Laurent, D. Forge, M. Port, A. Roch, C. Robic, L. V. Elst and R. N. Muller, *Chem. Rev.*, 2008, **108**, 2064─2110.
7. L. Zhang, W. ─F. Dong and H. ─B. Sun, *Nanoscale*, 2013, **5**, 7664─7684.
8. P. H. Mutin, G. Guerrero and A. Vioux, *J. Mater. Chem.*, 2005, **15**, 3761─3768.
9. J. Kim, J. E. Lee, S. H. Lee, J. H. Yu, J. H. Lee, T. G. Park and T. Hyeon, *Adv. Mater.*, 2008, **20**, 478─483.
10. T. Gillich, C. Acikgöz, L. Isa, A. D. Schlüter, N. D. Spencer and M.Textor, *ACS Nano*, 2013, **22**, 316–329.
11. J. Tang, M. Myers, K. A. Bosnick and L. E. Brus, *J. Phys. Chem. B*, 2003, **107**, 7501–7506.
12. H. Yu, M. Chen, P. M. Rice, S. X. Wang, R. L. White and S. Sun, *Nano Lett.*, 2005, **5**, 379–382
13. S. Tsunekawa, T. Fukuda and A. Kasuya, *J. Appl. Phys.*, 2000, **87**, 1318–1321.
14. B. Gilbert, J. E. Katz, J. D. Denlinger, Y. Yin, R. Falcone and G. A. Waychunas, *J. Phys. Chem. C*, 2010, **114**, 21994–22001.
15. M. Ali, S. Bora and S. K. Ghosh, *Langmuir*, 2014, **30** (34), 10449–10455.
16. W. Zhang, X. Li, R. Zou, H. Wu, H. Shi, S. Yu and Y. Liu, *Sci. Rep.*, 2015, **5**, 1─9.
17. C. Cunha, S. Panseri, D. Iannazzo, A. Piperno, A. Pistone, M. Fazio, A. Russo, M. Marcacci and S. Galvagno, *Nanotechnology*, 2012, **23**, 465102 1─5.
18. C. M. Julien and M. Massot, *J. Phys.: Condens. Matter*, 2003, **15**, 3151─3162.
19. M. Kim, X. M. Chen, Y. I. Joe, E. Fradkin, P. Abbamonte, and S. L. Cooper, *Phys. Rev. Lett.*, 2010, 104, 136402 1─3.

20. G. C. Silva, V. S. T. Ciminelli, A. M. Ferreira, N. C. Pissolati, P. R. P. Paiva and J. L. López, *Mater. Res. Bull.*, 2014, **49**, 544─551.
21. R. E Dinnebier and S. J. L. Billingue, In *Powder Diffraction Theory and Practice,* 1st edn., The Royal Society Chemistry, London, UK, 2008, p. 604.
22. U. Nobbmann and A. Morfesis, *Mater. Today*, 2009, **12**, 52─54.
23. R. M. Cornell and U. Schwertmann, In *The Iron Oxides*, 2nd edn., VCH:Weinheim, 2003.
24. C. Hui, C. Shen, T. Yang, L. Bao, J. Tian, H. Ding, C. Li and H. ─J. Gao, *J. Phys. Chem. C*, 2008, **112**, 11336─11339.
25. C. Ray, S. Dutta, Y. Negishi and T. Pal, *Chem. Commun.*, 2016, **52**, 6095–6098.
26. H. ─P. Cong and S. ─H. Yu, *Adv. Funct. Mater.,* 2007, **17**, 1814─1820.
27. J. Li, Y. Hu,W. Sun, Y. Luo, X. Shi and M. Shen, *RSC Adv.*, 2016, **6**, 35295─35304.
28. T. R. Cook, D. K. Dogutan, S. Y. Reece, Y .Surendranath, T. S. Teets and D. G .Nocera, *Chem. Rev*. 2010, **110**, 6474–6502.
29. P. V. Kamat, *J. Phys. Chem. C*, 2007, **111**, 2834–2860.
30. D. L. S. Rodney, S. Mathieu, R. D. Prévot, Z. Z. Fagan, A. S. Pavel, M. K. J. Siu, T. Simon and P. B. Curtis, *Science*, 2013, **340**, 60–63.
31. A. Iyer, J. Del-Pilar, C. K. King'ondu, E. Kissel, H. F. Garces, H. Huang, A. M. El-Sawy, P. K. Dutta and S. L. Suib *J. Phys. Chem. C,* 2012, **116**, 6474–6483
32. Y.Tang and W. Cheng, *Langmuir*, 2013, **29**, 3125−3132.
33. W. J. Youngblood, S. –H. Anna Lee, Y. Kobayashi, A. Emil, Hernandez-Pagan, G. H. Paul, A. M. Thomas, L. M. Ana, G. Devens and E. M. Thomas, *J. Am. Chem. Soc*., 2009, **131**, 926–927.
34. W. J. Youngblood, S. –H. Anna Lee, Y. Kobayashi, A. Emil, Hernandez-Pagan, G. H. Paul, A. M. Thomas, L. M. Ana, G. Devens and E. M. Thomas, *J. Am. Chem. Soc*.**,** 2009, **131**, 926–927.
35. L. Cheng, W. J. Huang, Q. F. Gong, C. H. Liu, Z. Liu, Y. G. Li and H. J. Dai, *Angew. Chem. Int. Ed.*, 2014, **53**, 7860–7863.
36. W. Rutherford, A. M. Thomas, *Nature*, 2008, **453**, 449.
37. S. M. Barnett, K. I. Goldberg and J .M. Mayer, *Nat. Chem*., 2012, **4**, 498–502.
38. M. R. Gao, W .C. Sheng, Z. B. Zhuang, Q. R. Fang, S. Gu, J. Jiang and Y. S. Yan, *J. Am. Chem Soc*., 2014, **136**, 7077–7084.

39. D. Kang, T. W. Kim, S. R. Kubota, A. C. Cardiel, H. G. Cha, and K. –S. Choi, *Chem. Rev.*, 2015, **115**, 12839–12887.
40. M. W. Kanan and D. G. Nocera, *Science*, 2008, **321**, 1072–1075.
41. J. D. Blakemore, R. H. Crabtree and G. W. Brudvig, *Chem. Rev.*, 2015, **115**, 12974–13005.
42. D. Holger, C. Limberg, T. Reier, M. Risch, S. Roggan and P. Strasser, *ChemCatChem*, 2010, **2**, 724–761.
43. M. Wiechen, M. M. Najafpour, S. I. Allakhverdiev and L. Spiccia, *Energy Environ. Sci.*, 2014, **7**, 2203–2212.
44. C. –H. Kuo, M. M. Islam, S. P. Altug, B. Sourav, A. M. El-Sawy, S. Wenqiao, Z. Luo, S.-Yu Chen, J. F. Rusling, H. Jie and S. L. Suib, *ACS Catal.*, 2015, **5**, 1693–1699.
45. C. E. Frey and K. Philipp, *Chem. Eur. J*., 2015, **21**, 14958–14968.
46. M. M. Najafpour, R. Gernot, H. Małgorzata, N. M. Atefeh, E. –M. Aro, R. Carpentier, N. Hiroshi, J. E. –R. Julian, J. R. Shen, I. A. Suleyman, *Chem. Rev.*, 2016, **116**, 2886–2936.
47. R. J. K. Taylor, M. Reid, J. Foot and S. A. Raw, *Acc. Chem. Res.*, 2005, **38**, 851–869.
48. I. Djerdj, A. Denis, J. Zvonko, M. Niederberger, *J. Phys. Chem. C* 2007, **111**, 3614–3623.
49. C. He, X. Wu and Z. He, *J. Phys. Chem. C*, 2014, **118**, 4578–4584.
50. J. Liu, J. Jiang, M. Bosman and J. F. Hong, *J. Mater. Chem.*, 2012, **22**, 2419–2426.
51. Y. Gorlin and F. J. Thomas, *J. Am. Chem. Soc.*, 2010, **132**, 13612–13614.
52. S. Hirai, Y. Goto, Y. Sakai, A. Wakatsuki, Y. Kamihara and M. Matoba, *J. Phys. Soc. Jpn.*, 2015, **84**, 1–6.
53. Y. M. Lee, C.-H. Hsu and H. −W. Chen, *Appl. Surf. Sci.*, 2009, **255**, 4658−4663.
54. S. Tsunekawa, T. Fukuda and A. Kasuya, *J. Appl. Phys.*, 2000, **87**, 1318–1321.
55. R. J. O. Mossanek, G. Domínguez-Cañizares, A. Gutiérrez, M. Abbate, D. Díaz-Fernández and L Soriano, *J. Phys. Condens. Matter* 2013, **25**, 495506 1−7.
56. R. W. Johnston and D. C. Cronemeyer, *Phys. Rev.*, 1954, **93**, 634−635; M. Zhou, L. Zhang, L. Shao, W. Wang, K. Fan and Q. Qizong, *J. Phys. Chem. A*, 2001, **105**, 5801–5807.

57. H. Guan, C. Shao, S. Wen, B. Chen, J. Gong and X. Yang, *Inorg. Chem. Commun*. 2003, **6**, 1302−1303; P. S. Patil and L. D. Kadam, *Appl. Surf. Sci.* 2002, **199**, 211−221.
58. J. Huang, Z. Yang, Z. Feng, X. Xie and X. Wen, *Sci. Rep.*, 2016, **6**, 24471 1−12.
59. A. Giri, N. Goswami, M. Pal, M. Tay, Z. Myint, S. Al-Harthi, A. Singha, B. Ghosh, J. Dutta and S. K. Pal, *J. Mater. Chem. C*, 2013, **1**, 1885–1895.
60. H. Long, T. Sh, H. Hu, S. Jiang, S. Xi and Z. Tang, *Sci. Rep.*, 2014, **4**, 7413–7422.
61. P. Li, C. Nan, Z. Wei, J. Lu, P. Qing and Y. Li, *Chem. Mater.*, 2010, **22**, 4232–4236.
62. Y. Ren, P. G. Bruce and Z. Ma, *J. Mater. Chem*., 2011, **21**, 9312–9318.
63. D. L. S. Rodney, S. Mathieu, R. D. Prévot, Z. Z. Fagan, A. S. Pavel, M. K. J. Siu, T. Simon and P. B. Curtis, *J. Am. Chem. Soc*., 2013, **135**, 11580−11586.
64. T. Ahmad, K.V. Ramanujachary, S. E. Lofland and A. K. Ganguli, *J. Mater. Chem.*, 2004, **14**, 3406–3410.
65. T. Alammar, O. Shekhah, J. Wohlgemuth and A. –V. Mudring, *J. Mater. Chem.*, 2012, **22**, 18252−18260.
66. H. –P. Cong and S. –H. Yu, *Adv. Funct. Mater.*, 2007, **17**, 1814–1820.
67. M. Zhang, M. de Respinis and H. Frei, *Nature Chem*., 2014, **6**, 362–367.
68. E. Laviron, *J. Electroanal. Chem*., 1979, **101**, 19–28.
69. A. J. Esswein and D. G. Nocera, *Chem. Rev*., 2007, **107**, 4022–4047.
70. M. W. Kanan, Y. Surendranath and D. G. Nocera, *Chem. Soc. Rev.* 2009, **38**, 109–114.